

# Anomalous low doping phase of the Hubbard model

C. Gröber, R. Eder and W. Hanke

*Institut für Theoretische Physik, Universität Würzburg, Am Hubland, 97074 Würzburg, Germany*  
(November 1, 2018)

We present results of a systematic Quantum-Monte-Carlo study for the single-band Hubbard model. Thereby we evaluated single-particle spectra (PES & IPES), two-particle spectra (spin & density correlation functions), and the dynamical correlation function of suitably defined diagnostic operators, all as a function of temperature and hole doping. The results allow to identify different physical regimes. Near half-filling we find an anomalous ‘Hubbard-I phase’, where the band structure is, up to some minor modifications, consistent with the Hubbard-I predictions. At lower temperatures, where the spin response becomes sharp, additional dispersionless ‘bands’ emerge due to the dressing of electrons/holes with spin excitations. We present a simple phenomenological fit which reproduces the band structure of the insulator quantitatively. The Fermi surface volume in the low doping phase, as derived from the single-particle spectral function, is not consistent with the Luttinger theorem, but qualitatively in agreement with the predictions of the Hubbard-I approximation. The anomalous phase extends up to a hole concentration of  $\approx 15\%$ , i.e. the underdoped region in the phase diagram of high- $T_c$  superconductors. We also investigate the nature of the magnetic ordering transition in the single particle spectra. We show that the transition to an SDW-like band structure is not accomplished by the formation of any resolvable ‘precursor bands’, but rather by a (spectroscopically invisible) band of spin 3/2 quasiparticles. We discuss implications for the ‘remnant Fermi surface’ in insulating cuprate compounds and the shadow bands in the doped materials.

71.10.Hf,71.10.Fd,75.40.Gb

## I. INTRODUCTION

The 1-band Hubbard model on a two-dimensional square lattice has the Hamiltonian

$$H = -t \sum_{\langle i,j \rangle, \sigma} (c_{i,\sigma}^\dagger c_{j,\sigma} + h.c.) + U \sum_i (n_{i,\uparrow} - \frac{1}{2})(n_{i,\downarrow} - \frac{1}{2}) - \mu \sum_i (n_{i,\uparrow} + n_{i,\downarrow}). \quad (1)$$

Here,  $c_{i,\sigma}^\dagger$  ( $c_{i,\sigma}$ ) creates (annihilates) an electron with spin  $\sigma$  in a Wannier orbital centered at lattice site  $i$ . The particle density at each site is given by  $n_{i,\sigma} = c_{i,\sigma}^\dagger c_{i,\sigma}$ . The first sum for the kinetic energy is restricted to include only the hopping matrix element  $t$  between next-nearest neighbor sites  $\langle i, j \rangle$ . Periodic boundary conditions are used throughout the following work. The second sum describes for  $U > 0$  an on-site Coulomb repulsion between particles of opposite spin that share the same lattice site. In the present work we restrict ourselves to  $U = 8.0t$ . The chemical potential  $\mu$  in the third sum controls the occupation of the finite lattice in the finite-temperature grand canonical Quantum-Monte-Carlo (QMC) simulation we performed. At half-filling, particle-hole symmetry of the kinetic and  $U$ -term implies  $\mu = 0$ . The analytic continuation of the dynamic imaginary-times QMC data to the real frequency axis is performed with state-of-the-art Maximum-Entropy (ME) techniques. For exhausting discussions concerning the QMC and ME methods we refer the reader to [1–3].

The 1-band Hubbard model exhibits several energy scales: in the repulsive case the high-energy scale  $U$  is important in determining the insulating gap at half-filling,  $\langle n \rangle = 1.0$ . An important low-energy scale is set by the exchange interaction  $J = 4t^2/U$ : in second order perturbation theory two particles with different spins on neighboring lattice sites can exchange via a virtual double occupation. This process is the source for the strong antiferromagnetic (AF) correlations found near and at half-filling.

With the exception of some known symmetry properties like invariance under global spin-rotation, whose generators form the  $SU(2)$ -algebra, and invariance under  $U(1)$ -transformation, i.e., charge-conservation, as well as the particle-hole transformation, no rigorous results are known for the 1-band Hubbard model in two-dimensions [4]. The Mermin-Wagner theorem [5] prevents a long-range ordered state in a two-dimensional system for finite temperatures, but it is commonly believed that the ground state of the spin-1/2 Heisenberg antiferromagnet, i.e. the large- $U$  limit of the repulsive half-filled Hubbard model [6], shows long-range Néel order in two dimensions. Néel order results also in the weak-coupling limit [7,8], where the gap  $\Delta$  is due to a spin-density-wave (SDW) instability related to perfect nesting.

It might seem that due to the Mermin-Wagner theorem the physics of the ordered phase is out of reach for our numerical technique, which is limited to finite temperatures. However, one may assume that the system ‘effectively orders’ as soon as the spin-correlation length

becomes comparable to the system size. Due to the periodic boundary conditions the spin-correlation function  $\chi(\mathbf{r}) = (1/L^2) \sum_i \langle \vec{S}_i \cdot \vec{S}_{i+\mathbf{r}} \rangle$  is a periodic function of  $\mathbf{r}$  and if the value of this function at the maximum value  $|\mathbf{r}| = \sqrt{2L}$  (with  $L \equiv$  cluster size) is still appreciable, we may expect that the system is ‘effectively ordered’. A rough measure would be the spin-correlation length  $\zeta$ , obtained by fitting  $\chi(\mathbf{r})$  to the form  $a \cdot |\mathbf{r}|^b \cdot e^{-|\mathbf{r}|/\zeta}$ . Since the infinite system has the Néel temperature  $T = 0$ , the spin-correlation length diverges as  $T \rightarrow 0$  and we may expect that in a *finite* system  $\zeta$  becomes comparable to the cluster size  $L$  at a *finite* temperature which depends on the lattice size. Below this temperature we then expect that the system resembles the ordered phase, although the spin-rotation symmetry persists even in this case. In that sense, the finite size of the system creates an artificial ‘Néel temperature’ which, however, depends on  $L$  and  $U/t$  etc and has no real counterpart in the infinite system. This has to be kept in mind when discussing the results.

We proceed by discussing some known approximations to the Hubbard model. The ‘classical’ approximation to the Hubbard model is the so-called Hubbard-I approximation [10]. Its essence is the splitting of the electron annihilation operator into the two ‘eigenoperators’ of the interaction part:

$$\begin{aligned} c_{i,\sigma} &= c_{i,\sigma} n_{i,\bar{\sigma}} + c_{i,\sigma} (1 - n_{i,\bar{\sigma}}) \\ &= \frac{1}{\sqrt{2}} (d_{i,\sigma} + h_{i,\sigma}^\dagger), \end{aligned} \quad (2)$$

whence

$$\begin{aligned} [d_{i,\sigma}, H_U] &= \frac{U}{2} d_{i,\sigma}, \\ [h_{i,\sigma}^\dagger, H_U] &= -\frac{U}{2} h_{i,\sigma}^\dagger. \end{aligned} \quad (3)$$

The physical content of the Hubbard-I approximation, which neglects any spin-correlations, becomes clear by realizing [11] that the equations of motion in this approximation are completely equivalent to an ‘effective Hamiltonian’ for double occupancy-like particles  $d_{i,\sigma}^\dagger = (1/\sqrt{2}) c_{i,\sigma}^\dagger n_{i,\bar{\sigma}}$  and hole-like particles  $h_{i,\sigma}^\dagger = (1/\sqrt{2}) c_{i,\sigma} (1 - n_{i,\bar{\sigma}})$ :

$$\begin{aligned} H &= -\frac{t}{2} \sum_{\langle i,j \rangle, \sigma} (d_{i,\sigma}^\dagger d_{j,\sigma} - h_{i,\sigma}^\dagger h_{j,\sigma}) \\ &\quad -\frac{t}{2} \sum_{\langle i,j \rangle, \sigma} (d_{i,\sigma}^\dagger h_{j,\bar{\sigma}}^\dagger + h.c.) \\ &\quad + \frac{U}{2} \sum_{i,\sigma} (d_{i,\sigma}^\dagger d_{i,\sigma} - h_{i,\sigma}^\dagger h_{i,\sigma}). \end{aligned} \quad (4)$$

This Hamiltonian contains terms which describe the pair creation of a hole and a double occupancy on nearest neighbors  $\langle i, j \rangle$ , terms which describe the propagation

of these effective particles, and an additional energy of formation of  $U$  for the double occupancy. The matrix elements for the propagation are reduced by a factor of  $1/2$ , because in an uncorrelated spin-background there is a probability of  $1/2$  for the spin on a nearest neighbor to have the proper direction to allow for the hopping of an electron. Solving (4) by Fourier and Bogoliubov transform:

$$\begin{aligned} \gamma_{1,\mathbf{k},\sigma} &= u_{\mathbf{k}} d_{\mathbf{k},\sigma} + v_{\mathbf{k}} h_{-\mathbf{k},\bar{\sigma}}^\dagger, \\ \gamma_{2,\mathbf{k},\sigma} &= -v_{\mathbf{k}} d_{\mathbf{k},\sigma} + u_{\mathbf{k}} h_{-\mathbf{k},\bar{\sigma}}^\dagger, \end{aligned} \quad (5)$$

yields the standard dispersion relation, which consists of the upper and lower Hubbard bands:

$$E_{\pm}^{Hub-I}(\mathbf{k}) = \frac{1}{2} \left( \epsilon_{\mathbf{k}} \pm \sqrt{\epsilon_{\mathbf{k}}^2 + U^2} \right). \quad (6)$$

Here  $\epsilon_{\mathbf{k}}$  denotes the free tight-binding dispersion  $\epsilon_{\mathbf{k}} = -2t(\cos(k_x) + \cos(k_y))$ . Using (2) we also obtain the correct spectral weights of the two Hubbard bands:

$$\begin{aligned} Z_{\pm}^{Hub-I}(\mathbf{k}) &= \frac{1}{2} (u_{\mathbf{k}} \pm v_{\mathbf{k}})^2 \\ &= \frac{1}{2} \left( 1 \pm \frac{\epsilon_{\mathbf{k}}}{\sqrt{\epsilon_{\mathbf{k}}^2 + U^2}} \right). \end{aligned} \quad (7)$$

As noted above, the key assumption in the Hubbard I approximation is the neglect of spin-correlations. Therefore, we expect that this approximation will become inaccurate as soon as spin-correlations become sufficiently strong so as to appreciably influence the propagation of holes and double occupancies. This effect will be strongest in the Néel ordered phase believed to be realized in the ground state. If we choose the ‘spin-background’, in which the holes and double occupancies propagate, to be the Néel state, the double occupancy  $d_{i\uparrow}^\dagger$  with spin  $\uparrow$  can exist only on the  $\downarrow$  sublattice and vice versa. Similarly, a hole  $h_{i\downarrow}^\dagger$  can be created only on the  $\downarrow$  sublattice and vice versa. We, thus, expect that we have to modify the Hubbard-I Hamiltonian (4) into:

$$\begin{aligned} H &= -t \sum_{i \in A, j \in N(i)} (d_{i,\uparrow}^\dagger h_{j,\uparrow}^\dagger + h.c.) \\ &\quad -t \sum_{i \in B, j \in N(i)} (d_{i,\downarrow}^\dagger h_{j,\downarrow}^\dagger + h.c.) \\ &\quad + \frac{U}{2} \sum_{i,\sigma} (d_{i,\sigma}^\dagger d_{i,\sigma} - h_{i,\sigma}^\dagger h_{i,\sigma}), \end{aligned} \quad (8)$$

where  $A$  ( $B$ ) denotes the  $\downarrow$  ( $\uparrow$ ) sublattice and  $N(i)$  denotes the set of nearest neighbors of site  $i$ . Note that the  $d_{i,\sigma}^\dagger d_{j,\sigma}$  and  $h_{i,\sigma}^\dagger h_{j,\sigma}$  propagation terms drop out (because of the  $A$  and  $B$  sublattices), and the matrix element for pair creation are  $t$  rather than  $t/2$  - this takes into account the fact that the spins on neighboring sites are

antiparallel with probability 1 rather than 1/2 as was the case in the paramagnetic state. Fourier and Bogoliubov transformation of (8) yields the dispersion

$$E_{\pm}^{SDW}(\mathbf{k}) = \pm \sqrt{\epsilon_{\mathbf{k}}^2 + \frac{U^2}{4}}, \quad (9)$$

and using

$$\begin{aligned} c_{\mathbf{k},\uparrow} &= h_{\mathbf{k},\uparrow} + d_{-\mathbf{k},\downarrow}^{\dagger} \\ c_{\mathbf{k}+\mathbf{Q},\uparrow} &= h_{\mathbf{k},\uparrow} - d_{-\mathbf{k},\downarrow}^{\dagger} \end{aligned} \quad (10)$$

(where  $\mathbf{k}$  is within the AF Brillouin zone), we find the spectral weight of these bands:

$$\begin{aligned} Z_{\pm} &= \frac{1}{2}(u_{\mathbf{k}} \pm v_{\mathbf{k}})^2 \\ &= \frac{1}{2} \left( 1 \pm \frac{\epsilon_{\mathbf{k}}}{\sqrt{\epsilon_{\mathbf{k}}^2 + \frac{U^2}{4}}} \right). \end{aligned} \quad (11)$$

This is precisely what is obtained from the SDW mean-field treatment of the Hubbard model by setting the staggered magnetization  $m$  to a value of 1 (which is a good approximation in the limit of large  $U$ ). In general, the SDW mean-field approximation models the AF Néel state by assuming  $\langle n_{i,\sigma} \rangle = \frac{1}{2}(1 + \sigma m e^{i\mathbf{Q}\mathbf{R}_i})$  with AF nesting vector  $\mathbf{Q} = (\pi, \pi)$  and staggered magnetization  $m = e^{i\mathbf{Q}\mathbf{R}_i} \langle n_{i,\uparrow} - n_{i,\downarrow} \rangle$  [7,8]. This results in the two-band dispersion

$$E_{\pm}^{SDW}(\mathbf{k}) = \pm \sqrt{\epsilon_{\mathbf{k}}^2 + \Delta^2}, \quad (12)$$

and the spectral weight

$$Z_{\pm}^{SDW}(\mathbf{k}) = \frac{1}{2} (1 \pm \epsilon_{\mathbf{k}}/E_{\pm}^{SDW}(\mathbf{k})). \quad (13)$$

The gap parameter is  $\Delta = Um/2$  and the staggered magnetization  $m$  is determined self-consistently from the following equation:

$$m = \frac{2}{N} \sum_{\mathbf{k}}^{\text{occupied}} \frac{Um}{\sqrt{(\epsilon_{\mathbf{k}} - \epsilon(\mathbf{k} + \mathbf{Q}))^2 + m^2 U^2}}. \quad (14)$$

The solution of this self-consistency equation yields the value  $\Delta = 3.56t$  at  $U = 8.0t$ , the value used in the present work. If we set  $m = 1$  on the other hand, as would be appropriate for  $U/t \rightarrow \infty$ , we obviously recover the results from our Hubbard-I-like Hamiltonian (8).

In the two limiting cases of no spin-correlations and of perfect Néel order we can thus treat the Hubbard model in a quite analogous fashion and, as will be seen below, the Hubbard-I results are indeed a good approximation to the actual spectral function in the limit of high temperature. The main problem then is how to describe the effect of spin-fluctuations and how to manage

the crossover from the completely disordered to the Néel ordered phase. Below, we will address this crossover by QMC simulations.

Thereby we want to take advantage of the possibility to calculate the spectra of specifically designed ‘diagnostic operators’. The first one of these is the ‘shadow’ operator:

$$\begin{aligned} \tilde{c}_{i,\sigma} &= c_{i,\sigma} n_{i,\bar{\sigma}} - c_{i,\sigma} (1 - n_{i,\bar{\sigma}}) \\ &= \frac{1}{\sqrt{2}} (d_{i,\sigma} - h_{i,\sigma}^{\dagger}). \end{aligned} \quad (15)$$

We note first of all, that the Fourier transform of this operator,  $\tilde{c}_{\mathbf{k},\sigma}$  has precisely the same quantum numbers as the ordinary electron operator  $c_{\mathbf{k},\sigma}$ : momentum  $-\mathbf{k}$ , total spin 1/2,  $z$ -spin  $\sigma$ , and identical point group symmetry at high symmetry momenta. It follows that the poles in its dynamical correlation functions

$$A_{\tilde{c}}(\mathbf{k}, \omega) = \sum_{\nu} |\langle \Psi_{\nu} | \tilde{c}_{\mathbf{k},\sigma} | \Psi_{\mu} \rangle|^2 e^{-\beta(E_{\mu} - E_{\nu})} \delta(\omega - (E_{\nu} - E_0)) \quad (16)$$

originate from exactly the same final states  $|\Psi_{\nu}\rangle$  as those of the photoemission spectrum. It can happen only accidentally that a given state  $\nu$  has an exactly vanishing weight in one of the correlation functions, but not the others. In this case, however, any arbitrarily small perturbation will remove the accidental vanishing of the peak. The only thing that can and will be different in the spectra of the diagnostic operator, are the *weights* of the peaks,  $|\langle \Psi_{\nu} | \tilde{c}_{\mathbf{k},\sigma} | \Psi_0 \rangle|^2$ . In fact, comparison of equations (11) and (7) shows immediately that both for the Hubbard I approximation and for the SDW-approximation use of the operator  $\tilde{c}_{\mathbf{k},\sigma}$  instead of  $c_{\mathbf{k},\sigma}$  exchanges the weights of the two Hubbard/SDW bands. It follows that band portions which have a small spectral weight in the spectra of the ordinary electron operator will acquire a large spectral weight in the spectrum of  $\tilde{c}_{\mathbf{k},\sigma}$  and vice versa. Therefore, this diagnostic operator is a useful tool to map out the ‘shadowy’ parts of the spectra in the outer parts of the Brillouin zone. An additional benefit is that since the ME technique resolves peaks with large spectral weight more reliably than those with small weight, we can get more precise information about the dispersion of these bands with weak intensity. The second diagnostic operator that we will be using is the ‘spin-1/2 string’ operator

$$\begin{aligned} b_{i,\uparrow} &= \sum_{j \in N(i)} (c_{i\uparrow} S_j^z + c_{i\downarrow} S_j^-), \\ b_{i,\uparrow}^{\dagger} &= \sum_{j \in N(i)} (c_{i\uparrow}^{\dagger} S_j^z + c_{i\downarrow}^{\dagger} S_j^+), \end{aligned} \quad (17)$$

where the sum on the r.h.s. runs over the nearest neighbors  $j$  of site  $i$ . This operator is the Clebsch-Gordan contraction of the adjoint rank-1 spinor  $c_{i,\sigma}$  and the spin-1 vector operator  $\vec{S}_j$  into yet another adjoint rank-1 spinor.

It describes the annihilation of a ‘dressed’ electron, i.e., an electron with a spin-excitation on a nearest neighbor. Again, since the Fourier transforms of the diagnostic operator,  $b_{\mathbf{k},\sigma}$ , agrees with the electron annihilation operator  $c_{\mathbf{k},\sigma}$  in all conceivable quantum numbers (momentum, total spin,  $z$ -component of the spin, point group operations in the case of high symmetry momenta), it obeys precisely the same selection rules, whence it is just as good as the  $c$ -operator itself to map out the band structure.

One further point, which is important from the technical point of view, is the following: under the particle-hole transformation  $c_{i,\sigma} \rightarrow e^{i\mathbf{Q}\cdot\mathbf{R}_i} c_{i,\sigma}^\dagger$  we have  $\tilde{c}_{i,\uparrow} \rightarrow -e^{i\mathbf{Q}\cdot\mathbf{R}_i} \tilde{c}_{i,\uparrow}^\dagger$  and  $b_{i,\uparrow} \rightarrow -e^{i\mathbf{Q}\cdot\mathbf{R}_i} b_{i,\uparrow}^\dagger$ . This implies that at half-filling the spectra of the shadow and spin-1/2 string operator obey the same particle-hole-symmetry as those of the ordinary electron operator, i.e.

$$A(\mathbf{k}, \omega) = A(\mathbf{k} + \mathbf{Q}, -\omega). \quad (18)$$

In our MaxEnt program particle-hole-symmetry is not implemented as an additional constraint, in other words: the MaxEnt procedure does not ‘know’ about this additional symmetry. The degree to which (18) is obeyed in the final spectra thus gives a good check for the accuracy of the reconstructed spectra. This is of particular importance in the case of the spin-1/2 string operator because the Wick-contraction of this operator on any given time slice produces a total of  $\approx 80$  products of noninteracting Green’s functions. The computation is, therefore, much more prone to inaccuracies so that an additional check is desirable.

The present work is organized as follows: first, we compare the temperature dependent dynamic single-particle properties of the Hubbard model with the predictions of the mean-field SDW and Hubbard-I approximations. In addition, we consider the temperature dependent two-particle excitations. Then, we will use our first diagnostic operator, the shadow operator  $\tilde{c}_{\mathbf{k},\sigma}$ , to show the existence of a total of four bands in the photoemission spectrum and to shed light onto the temperature dependent crossover from the SDW to the Hubbard-I regime. Then we will investigate the 4-band structure in more detail: after a phenomenological fit, which is able to produce a total of four bands, we will consider the string picture which naturally leads to our second diagnostic operator, the spin-1/2 string operator  $b_{\mathbf{k},\sigma}$ . This operator will be used to ultimately reveal the underlying mechanisms behind the generation of the 4-band structure, namely the dressing of the photoholes by clouds of AF spin-excitations. To resolve the ‘AF mirror image’ of the narrow quasiparticle spectral weight features between  $\mathbf{k} = (0, 0)$  and  $\mathbf{k} = (\pi, 0)$  around momentum  $\mathbf{k} = (\pi, \pi)$  we introduce also a spin-3/2 string operator. Finally, we will concentrate on the doped regime, thereby showing the violation of the Luttinger theorem near half-filling,

and discuss the hole concentration range in which these dressing effects dominate the low-energy physics.

## II. TEMPERATURE DEPENDENT DYNAMICS AT HALF-FILLING

We start in figure 1 with the discussion of the angle-resolved single-particle spectral function  $A(\mathbf{k}, \omega)$  for  $U = 8.0t$  and various temperatures in the range from  $T = 4.00t$  to  $T = 0.10t$ . In the left column of the figure the spectral functions are shown as ‘grey-scale’ plots versus momentum  $\mathbf{k}$  and energy  $\omega/t$  with dark (light) areas corresponding to large (small) spectral weight. The same spectra are shown also in the right column, but now as line-plots at each momentum  $\mathbf{k}$ . The QMC data in the figure are compared to the renormalized results of the Hubbard-I approximation at high and medium temperatures and with the renormalized results of the mean-field SDW approximation at the lowest temperature,  $T = 0.10t$ . ‘Renormalized’ means here that we have readjusted the parameters  $U$  and  $t$  in (6) and (12) so as to obtain an optimal fit to the ‘bands’ of high spectral weight in the spectra. These approximate dispersions are plotted as solid lines in the left column, while their spectra are shown in the right column as line-plots at each momentum  $\mathbf{k}$ . Thereby we have assumed a Lorentzian lineshape with a suitably chosen temperature dependent width (the Hubbard-I approximation does not provide any information about linewidths).

Starting at the highest calculated temperature,  $T = 4.00t$ , we find that the Hubbard-I approximation with practically unrenormalized parameters ( $\tilde{t} = 0.95t$  and  $\tilde{U} = 8.32t$ ) fits the QMC spectral functions almost perfectly regarding both the general dispersion and the distribution of spectral weight (quadratic deviation per degree of freedom  $\chi^2 = 0.05$ ). This is not surprising since the Hubbard-I approximation is derived for the paramagnetic state thereby neglecting all effects of spin-correlations, i.e., the Hubbard-I approximation essentially describes the interplay between itinerant electrons and strong on-site repulsion. This should be a reasonable assumption at this high temperature since all relevant spin-degrees of freedom are thermally excited.

Lowering the temperature to  $T = 1.00t$  and further to  $T = 0.33t$ , the data show that the Hubbard-I approximation increasingly fails to reproduce the entire spectrum and is only able to fit the peaks with maximal spectral weight reasonably well. Even then, in order to achieve these fits, one already has to renormalize the free parameters strongly. The values we found are  $\tilde{t} = 1.38t$  and  $\tilde{U} = 5.57t$  with  $\chi^2 = 1.54$  at  $T = 1.00t$  and  $\tilde{t} = 1.40t$  and  $\tilde{U} = 3.96t$  with  $\chi^2 = 0.85$  at  $T = 0.33t$ . The peaks that are missed by the Hubbard-I approximation are the states that form the first ionization/affinity states around momentum  $\mathbf{k} = (0, 0)/(\pi, \pi)$  on the photoemission/inverse

photoemission side and two rather dispersionless bands at higher energies of  $\omega \approx \pm 6.0t$ . The former states were previously resolved by Preuss and co-workers [12]. Altogether one can distinguish a total of four ‘bands’ in the single particle spectral density. As will be seen below, the temperature/doping regime where this 4-band structure is seen coincides with the regime where a collective low-energy mode with momentum  $(\pi, \pi)$  in the spin-response exists. In spite of this, however, we stress that the 4-band structure cannot be explained by a back-folding of the band structure due to ordering effects since the spin-correlation length is  $\leq 1.5$  lattice spacings at temperatures  $T \geq 0.33t$ .

For the lowest temperature,  $T = 0.10t$ , the QMC data are compared with the results from the AF SDW approximation. As in the case of the Hubbard-I approximation at medium temperatures, the lowermost spectra of figure 1 show that the SDW approximation is only able to fit the peaks with large spectral weight. Again one has to renormalize the free parameters heavily to values of  $\tilde{t} = 1.34t$  and  $\tilde{\Delta} = 2.29t$  with  $\chi^2 = 0.83$ . Moreover, as was the case for the Hubbard-I approximation at higher temperatures, the SDW approximation neither explains the states that form the first ionization/affinity states around momentum  $\mathbf{k} = (0, 0)/(\pi, \pi)$  on the photoemission/inverse photoemission side, nor the two dispersionless bands at higher excitation energies which can be seen rather clearly in the spectra.

All in all, the overall distribution of spectral weight is roughly reproduced by the Hubbard-I and SDW approximations as long as one forgets about the 4-band structure. In fact it is well known that the *integrated* photoemission or inverse photoemission weight (that means the electron momentum distribution) at each  $\mathbf{k}$ -point is reproduced quite well by the Hubbard-I approximation and the related 2-pole approximation [13].

As already mentioned, the emerging of the 4-band structure in the photoemission somewhere in between  $T = 1.00t$  and  $T = 0.33t$  is closely related to a change in the spin-response: to illustrate this we consider figure 2, which shows the spin-correlation function,  $\chi_{sz}(\mathbf{k}, \omega)$  (left column), and the charge-correlation function,  $\chi_{cc}(\mathbf{k}, \omega)$  (right column), for different temperatures. Whereas the spin-response is entirely incoherent at  $T = 1.00t$ , with decreasing temperature it can be fitted increasingly well by the spin-wave dispersion

$$E^{SW}(\mathbf{k}) = 2J\sqrt{1 - \frac{1}{4}(\cos(k_x) + \cos(k_y))^2}. \quad (19)$$

This result is known from previous calculations [7,8], which demonstrated that the two-particle correlation functions like the spin-response can be described within the SDW approximation even for large values of the interaction  $U$ . The energy scale  $J$  directly manifests itself in the spin-response since the spin-wave dispersion takes the value of  $E^{SW}(\pi, 0) = 2J$  at momentum  $\mathbf{k} = (\pi, 0)$ .

The fit parameters are  $\tilde{J} = 0.33t$  with  $\chi^2 = 0.01$  at  $T = 0.33t$  and  $\tilde{J} = 0.49t$  with  $\chi^2 = 0.11$  at  $T = 0.10t$ . The latter is already quite close to the strong coupling estimate  $J = 4t^2/U = 0.5t$ . Furthermore, the figure shows that with decreasing temperature the spin-response concentrates its weight more and more at the AF momentum  $\mathbf{Q} = (\pi, \pi)$  (as it is the case in AF spin-wave theory) and at a characteristic energy  $\omega^*$ . The latter decreases with decreasing temperature, i.e., the spin-response comes closer and closer to the predictions of AF spin-wave theory (19). The spin-correlation length  $\zeta_{sz}(T)$  can be derived from a real-space fit of the QMC equal-imaginary-times spin-correlation function  $\chi(\mathbf{r})$  to the form  $a \cdot |\mathbf{r}|^b \cdot e^{-|\mathbf{r}|/\zeta_{sz}(T)}$  thereby incorporating the effects of the periodic boundary conditions. While this is the best one can do on a finite lattice with periodic boundary conditions, the fit will only lead to roughly correct values due to the relative small system size of  $8 \times 8$ . The values obtained for the spin-correlation length then are  $\zeta_{sz} = 0.3 - 0.5$ ,  $\zeta_{sz} = 1.0 - 1.3$ ,  $\zeta_{sz} = 1.6 - 1.9$ ,  $\zeta_{sz} = 2.1 - 2.8$  and  $\zeta_{sz} > 8$  for  $T = 1.00t$ ,  $T = 0.33t$ ,  $T = 0.25t$ ,  $T = 0.20t$  and  $T = 0.10t$ , respectively. We actually believe that the spin-correlation length reaches the system size already at a temperature of  $T \approx 0.20t$ , because at this temperature the fit results in values between  $\zeta_{sz} = 2.1$  and  $\zeta_{sz} = 2.8$  (with the exponent  $b$  set to zero or not) but always with error bars of roughly the system size.

The charge-response  $\chi_{cc}(\mathbf{k}, \omega)$ , on the other hand, is rather broad in both momentum  $\mathbf{k}$  and energy  $\omega$  for all temperatures studied. Furthermore, the charge-response is gapped for temperatures below  $T \approx 1.00t$  and, therefore, can certainly not be responsible for any low-energy features of the single particle spectrum.

It is then quite obvious that at roughly the same temperature where the two narrow dispersive quasiparticle-like bands (that cannot be interpreted within the framework of the Hubbard-I or SDW approximations) appear in the single particle spectrum, the spin-response develops a sharp collective low-energy mode. We conclude that the underlying mechanism behind the occurrence of the 4-band structure consists in dynamical magnetic correlation effects, which are beyond the scope of the Hubbard-I and SDW approximations.

In the following, we want to explore the single particle spectrum by means of our *diagnostic operators*. The first of them is the shadow operator  $\tilde{c}_{i,\sigma}$  of equation (15) which will be used to transfer spectral weight from the inner parts of the Brillouin zone to the outer ones in case of normal photoemission  $\omega < \mu$ . As already discussed above, this also improves the resolution of the ME method in this region, since its resolution strongly depends on the spectral weight at a certain position. Nevertheless the spectrum of the shadow operator has to exhibit exactly the same peak positions as the normal photoemission spectrum.

Figure 3 shows the angle-resolved spectral function of the shadow operator for moderate and low temperatures. As expected, the shadow operator has its main spectral weight near  $\mathbf{k} = (\pi, \pi)$  on the photoemission side and near  $\mathbf{k} = (0, 0)$  on the inverse photoemission side. Furthermore, its spectrum supports the existence of a total of four bands, because it resolves a group of peaks forming dispersionless bands at energies of  $\omega \approx \pm 6.0t$ , a region where the normal photoemission spectrum exhibits only some weak and smeared-out spectral weight. These two dispersionless bands at energies of  $\omega \approx \pm 6.0t$  are inconsistent with the dispersions of the Hubbard-I and SDW approximations of figure 1. We will further address this topic later in this work.

Next, we turn in more detail to the temperature dependence of the photoemission spectrum. Figure 4 shows some close-ups of the normal photoemission spectrum and of the spectrum of the shadow operator at momentum  $\mathbf{k} = (\pi, \pi)$  and different temperatures. For the normal photoemission operator these close-ups show a peak at  $\omega \approx -1.5t$ , which would be consistent with Hubbard-I (see Figure 2). In the spectrum of the shadow operator this feature is visible as a single resolved peak only at the highest temperature,  $T = 1.00t$  whereas for temperatures down to  $T = 0.20t$  there is only some diffuse weight at this position. In the ordinary photoemission spectrum the peak loses spectral weight with decreasing temperature. It disappears completely at  $T < 0.20t$  where the spin-correlation length  $\zeta_{sz}(T)$  reaches the system size (see above). Thus, the temperature  $T \approx 0.20t$  where we lose the Hubbard-I-like peak at  $\omega \approx -1.5t$  and  $\mathbf{k} = (\pi, \pi)$  coincides quite accurately with the temperature where ‘effective’ long-range order sets in. Moreover, we find that as the normal photoemission spectrum loses the peak at  $\omega \approx -1.5t$  and  $\mathbf{k} = (\pi, \pi)$ , the spectrum of the shadow operator gains weight at  $\omega \approx -6.0t$ . Thus, we expect that both features are closely related to the temperature development of the spin-correlation length  $\zeta_{sz}(T)$ . We note, however, that the crossover in the shape of the dispersion from Hubbard-I-like to SDW-like occurs in a quite unexpected way: the topmost band at  $(\pi, \pi)$  does *not* deform into the SDW form in any continuous way, but simply ‘fades away’ and eventually vanishes at the transition.

A further surprising result is the following: at  $T = 0.10t$  neither the ordinary electron operator nor the shadow operator pick up the ‘AF umklapp band’ corresponding to the narrow dispersive band seen for example at  $\omega \approx -3t$  for  $\mathbf{k} = (0, 0)$ , i.e. there is no corresponding band at  $\omega \approx -3t$  and  $\mathbf{k} = (\pi, \pi)$ . Note that in the framework if the SDW-approximation the shadow operator *must* reproduce this umklapp-band at  $(\pi, \pi)$  with the *same weight* as the original band at  $(0, 0)$  in the ordinary photoemission spectrum - see the discussion in the first section. That this is not the case shows that even at this lowest temperature, a simple SDW-like descrip-

tion of the band structure is invalid, in that the band structure cannot be understood by simple backfolding of the spectrum obtained without broken symmetry. As we will see in the following the AF SDW state provides only the ‘background’ for the dressing of the photoholes with AF spin-excitations which dynamically generate a total of four bands.

### III. THE 4-BAND STRUCTURE

We return to the discrepancy between the 2-band dispersions of the Hubbard-I and SDW approximations and the 4-band structure actually observed for example in the spectrum of the shadow operator of figure 3.

In order to generate a ‘4-band structure’ out of the two bands of the Hubbard-I and SDW approximations we try as a phenomenological ansatz to mix the dispersions of the Hubbard-I/SDW approximation with two dispersionless bands at energies of  $E_{\pm} = \pm 3.0t$ . In other words, for both the photoemission and inverse photoemission spectrum we diagonalize an ‘effective’  $2 \times 2$  Hamilton matrix:

$$H_{\pm} = \begin{pmatrix} E_{\pm}^{Hub-I/SDW} & V \\ V & E_{\pm} \end{pmatrix}, \quad (20)$$

and plot in figure 5 the four bands obtained in this way on top of the spectral density obtained from QMC at  $T = 0.33t$  and  $T = 0.10t$ . For comparison the figure also shows the original (i.e. unhybridized) Hubbard-I bands plus the two phenomenological dispersionless bands at energies of  $\omega = \pm 3.0t$ . The figure shows that the overall agreement between the QMC peak positions and the four bands generated by diagonalizing  $H_{\pm}$  of equation (20) is surprisingly good, particularly so in view of the fact that for both, Hubbard-I and SDW approximation, only *unrenormalized* parameters were used. In particular, the *self-consistently* determined value for the SDW gap  $\Delta$  of  $3.56t$  was used at  $T = 0.10t$ . The only ‘external’ parameter in this figure is the mixing matrix element  $V$ , which was set to a value of  $1.0t$ .

Thus, we find in contrast to previous works [14], that the introduction of the dispersionless bands reproduces the single-particle gap and the width of the quasiparticle band correctly without any renormalization of parameters. Rather, the narrowing of the quasiparticle band and the reduction of the Hubbard gap as compared to the unrenormalized parameters is brought about by introduction of the dispersionless bands. This naturally raises the question as to their physical origin. In the present paper we restrict ourselves to a more phenomenological and ‘numerics based’ approach. A complementary and more mathematical discussion is given in Ref. [11], where an equation of motion approach similar to Hubbard’s original work is pursued.

We consider the commutator of the creation operator for

hole-like particles,  $h_{i,\sigma}^\dagger = c_{i,\sigma}(1 - n_{i,\bar{\sigma}})$ , which annihilates a particle only on a singly occupied site, with the kinetic energy of the Hubbard model and find [11]:

$$[h_{i,\uparrow}^\dagger, H_t] = -t \sum_{j \in N(i)} \left[ \left(1 - \frac{\langle n \rangle}{2}\right) c_{j,\uparrow} + (c_{j,\uparrow} S_i^z + c_{j,\downarrow} S_i^-) - \frac{1}{2} c_{j,\uparrow} (n_i - \langle n \rangle) + c_{j,\downarrow}^\dagger c_{i,\downarrow} c_{i,\uparrow} \right] \quad (21)$$

Keeping only the first term in the square brackets of equation (21) reproduces the Hubbard-I approximation [10]. The second term in the square brackets describes the dressing of the created hole by a spin-excitation and is closely related to the spin-1/2 string operator of equation (17). The third term describes in an analogous fashion the coupling of the hole to a density fluctuations, whereas the fourth term describes the coupling to the  $\eta$ -excitation [15]. The two latter types of excitation are not important for a large positive  $U$  near half-filling,  $\langle n \rangle = 1.0$ , and will be neglected. Therefore, the operator  $\sum_{j \in N(i)} (c_{j,\uparrow} S_i^z + c_{j,\downarrow} S_i^-)$  is in this case the most important correction over the Hubbard-I approximation. As already stated, it describes a hole dressed by a spin-excitation: this operator not only creates a hole on site  $j$  but dresses this hole with a spin-excitation on a neighboring site, which is exactly the idea behind the spin-bag [7,8] or spin-polaron [9] pictures known in the literature. Splitting this operator into eigenoperators of  $H_U$ :

$$\begin{aligned} \hat{C}_{i\uparrow} &= \sum_{j \in N(i)} (\hat{c}_{j,\uparrow} S_i^z + \hat{c}_{j,\downarrow} S_i^-), \\ \hat{D}_{i\uparrow} &= \sum_{j \in N(i)} (\hat{d}_{j,\uparrow} S_i^z + \hat{d}_{j,\downarrow} S_i^-), \end{aligned} \quad (22)$$

we find  $[\hat{D}_{i\sigma}, H_U] = \frac{U}{2} \hat{D}_{i,j,\sigma}$  and  $[\hat{C}_{i\sigma}, H_U] = -\frac{U}{2} \hat{C}_{i,j,\sigma}$ . Assuming moreover that the mobility of these composite excitations is determined by the ‘heavy’ spin-excitation, it seems quite reasonable to assume that these ‘particles’ are the source of the (more or less) dispersionless bands at  $\approx \pm U/2$ .

Finally, the commutation relation (21) shows that the mixing matrix element between the  $h_{\mathbf{k},\sigma}$  and the new composite particles should be  $\approx t$ . Based on these rough considerations we might thus expect that the two string-1 ‘effective particles’ (22) are excellent candidates for explaining the two dispersionless bands at  $\pm 3t$  required to upgrade the Hubbard-I or SDW approximation so as to match the QMC data. However, so far the above considerations are pure speculation and in the following we will turn to QMC-results to back up this hypothesis by numerical evidence.

Before doing so, however, we want to illustrate the action of the ‘string-operator’ in two extreme cases: an ideal Néel state and a resonating valence-bond (RVB) state, i.e. a compact singlet covering of the plane [4] (see figure 6). In the Néel state, a hole created initially on site  $i$  can

travel one place to a neighboring site  $j$  thereby leaving behind a misaligned spin on the original site  $i$ . Exactly this process is described by the second term,  $c_{j,\downarrow} S_i^-$ : it creates a hole of opposite spin on a neighboring site  $j$  and flips the spin on the original site  $i$ . Therefore, this process corresponds to the creation of a string of length 1. In fact one might think about more sophisticated diagnostic operators incorporating the effects of longer-ranged strings [16]. Indeed, Dagotto and Schrieffer [16] and Eder and Ohta [17] already measured the angle-resolved spectrum of a diagnostic operator containing strings with up to three lattice sites range by means of exact diagonalizations of the  $t - J$  model. As already mentioned in the introduction, in the QMC method each observable has to be expressed in terms of free single-particle Greens functions on each time slice by the application of Wick’s theorem [18]. This results already in a quite large expression for the spin-1/2 string operator of equation (17) containing approximately 80 contributions. The implementation of even longer-ranged string operators therefore was not possible.

Returning to the spin-1/2 string operator of equation (17) we note that the first term,  $c_{i,\uparrow} S_j^z$  will always annihilate a Néel state. This reflects the simple fact that spin-rotation symmetry is broken in the Néel state. This is not the case, however, in the fully rotationally invariant RVB state: again, creating a hole on site  $i$  and allowing it to hop to site  $j$  will produce a spin-excitation. However, in the case of the RVB state, it produces the superposition of two states: in one case the dotted ellipse stands for the  $S_z = -1$  component of the triplet, and this state would again be created by the term  $c_{j,\downarrow} S_i^-$ . There is, however, also a second state where the dotted ellipse corresponds to the superposition of a singlet and the  $S_z = 0$  component of the triplet. This second state then would be created by the term  $c_{i,\uparrow} S_j^z$ , whereby the relative sign of the two terms in the string-1 operator makes sure that the two configurations are always produced with the proper phase. In both extreme cases, Néel state and ‘singlet soup’, the string-1 operator thus creates a hole dressed with the proper spin-excitation: this can be a spin wave (i.e. a single inverted spin) in the case of a Néel state, or a singlet-triplet excitation in the case of an RVB state.

As a technical remark we still note that the excessive numerical effort which would have been necessary to compute spectra for the  $\hat{C}_{i,\sigma}$  and  $\hat{D}_{i,\sigma}$  (which are products of 5 Fermion operators) has made it impossible to compute the spectra of these operators - instead we have been using the (Fourier transform of) the operator  $b_{i,\uparrow}$ , defined in (17). Concerning the difference between this diagnostic operator and the operator  $\sum_{j \in N(i)} (c_{j,\uparrow} S_i^z + c_{j,\downarrow} S_i^-)$  obtained by commuting  $h_{i,\uparrow}^\dagger$  with the kinetic energy (see the second term on the r.h.s. of equation (21)), we note that their Fourier transforms differ only by phase factors of the form  $e^{-i\mathbf{k}(\mathbf{R}_i - \mathbf{R}_j)}$ . Both operators are indeed iden-

tical at momentum  $\mathbf{k} = (0, 0)$  and differ at momentum  $\mathbf{k} = (\pi, \pi)$  only by a factor of  $-1$  since  $\mathbf{R}_i$  and  $\mathbf{R}_j$  are next-nearest neighbor lattice sites. At all other momenta both operators have exactly the same peaks but will differ somewhat in their spectral weights.

After these remarks we discuss the angle-resolved spectral function of the spin-1/2 string operator  $b_{\mathbf{k}, \uparrow}$ , shown in figure 7. The spectrum of the spin-1/2 string operator indeed picks up those band portions which, according to the rough hybridization scenario in figure 5, should have strong ‘flat-band character’, i.e. the part of the narrow low energy band between  $(0, 0)$  and  $(\pi/2, \pi/2)$  and between  $(0, 0)$  and  $(\pi, 0)$  at energies  $\omega \approx -3t$ . We note that these are precisely the positions where the two quasiparticle-like dispersive narrow bands occurred in the normal photoemission spectrum at  $T = 0.33t$ . In addition, the band portion at  $\omega \approx -6t$  for momentum  $(\pi, \pi)$  is also enhanced in the string-1 spectrum.

This, however, still leaves an important part of the band structure unexplained. Namely, the ‘AF umklapp band’ of the narrow quasiparticle band dispersing upward between  $(0, 0)$  and  $(\pi/2, \pi/2)$  at  $\omega \approx -3t$  still is not seen in any of the spectra, not even at the lowest temperature studied. On the other hand, in a state with true antiferromagnetically broken symmetry we know that this mirror image must exist due to the backfolding of the Brillouin zone. To finally resolve this part, we now introduce the last diagnostic operator of this work, which we call the spin-3/2 string operator:

$$\tilde{b}_{i, \uparrow} = \sum_{j \in N(i)} (2c_{i, \uparrow} S_j^z - c_{i, \downarrow} S_j^-). \quad (23)$$

This describes again a composite object of a hole and a spin-excitation, but this time the two constituents are coupled to the total spin of 3/2. We stress that this operator will detect states which can never be seen in an actual angle-resolved photoemission spectrum on a singlet ground state, because this is forbidden by the angular-momentum selection rule. The angle-resolved spectral function  $\tilde{A}(\mathbf{k}, \omega)$  of the spin-3/2 string operator is plotted in figure 8 again for  $T = 0.33t$  (top) and  $T = 0.10t$  (bottom). It is then immediately obvious that it is this operator which resolves the ‘missing piece’ of the AF dispersion, i.e. the ‘AF mirror image’ of the narrow quasiparticle band. It should also be noted that the spectrum of  $\tilde{b}_{i, \uparrow}$  is remarkably independent of temperature, i.e. the states belonging to this ‘spin-3/2 band’ persist irrespectively of whether there is long-range order or not.

Combining the information obtained so far, suggests the following scenario for the crossover between the paramagnetic band structure at high temperature and the AF band structure at low temperature: in the paramagnetic state at high temperatures (such as  $T = 0.33t$ ), the spin is a good quantum number and the spin-3/2 ‘band’ does exist but cannot mix with any spin-1/2 band due

to spin-conservation. The band of spin-3/2 quasiparticles thus plays no role whatsoever in the actual photoemission spectrum, which is presumably the reason why the outer part of the spectrum is so remarkably ‘invisible’ in actual ARPES experiments, leading to the idea of a ‘remnant Fermi surface’ in the insulator [19]. Reaching this state by photoemission would only be possible if the photohole is created in a thermally admixed state of at least spin 1. In an infinite system this situation changes discontinuously at the transition to the true broken symmetry state: there the total spin ceases to be a good quantum number, and the spin-1/2 band in the interior of the AF zone and the spin-3/2 band in the exterior now suddenly can mix with each other, thus leading to the familiar SDW dispersion. We note that another way to generate a coupling between these two bands would be application of a magnetic field - this also would break spin-rotation invariance and hence enable the hybridization of a spin-1/2 and a spin-3/2 band. Based on our results we thus believe that a magnetic field could enhance the spectral weight of the ‘shadow part’ of the band structure as seen in ARPES.

#### IV. DOPING THE HUBBARD MODEL AT HIGH TEMPERATURES – RIGID BANDS

Summarizing our results so far, we may say that the Hubbard-I approximation, slightly improved by the introduction of new quasiparticles corresponding to dressed holes provides a very good description of the spectral function for the case of half-filling,  $\langle n \rangle = 1$ . In this section we want to proceed to the doped case  $\langle n \rangle < 1$ , which is of prime interest for cuprate superconductors. Here, an essential drawback of the QMC procedure is that reliable QMC simulations for lower temperatures are much more difficult or even impossible, since the absence of particle-hole symmetry away from half-filling introduces the notorious minus-sign problem into the algorithm. Truly low temperatures like  $T = 0.10t$ , which in principle correspond to the physical temperature range, are therefore out of reach. On the other hand in the study of the half-filled case we have seen that a major change takes place as the spin correlation length reaches the system size, whence ‘effective long range order’ sets in. In the doped case the spin correlation length is expected to be short at any temperature, whence we may expect that the change of  $A(\mathbf{k}, \omega)$  from high to small temperature is more smooth than at half-filling. In that sense, even  $A(\mathbf{k}, \omega)$  data for the relatively high temperature  $T = 0.33t$  are interesting to study. Moreover, we can at least try to elucidate trends with decreasing temperature and thus construct a reasonably plausible scenario.

At half-filling, we have seen that the ‘approximation of choice’ for the paramagnetic case was the Hubbard-I approximation. This naturally poses the question as to how

relevant the half-filled case is for the description of the doped case, i.e. how much of the Hubbard-I physics remains valid for finite doping. At half-filling the two ‘effective particles’  $\hat{d}_{i,\sigma}^\dagger$  and  $\hat{c}_{i,\sigma}^\dagger$ , form the two separate Hubbard bands. The effect of doping would now consist in the chemical potential cutting progressively into the top of the lower Hubbard band, in much the same fashion as in a doped band insulator. On the other hand, for finite  $U/t$  the spectral weight along this band deviates from the free-particle value of 1 per momentum and spin so that the Fermi surface volume (obtained from the requirement that the integrated spectral weight up to the Fermi energy be equal to the total number of electrons) is not in any ‘simple’ relationship to the number of electrons - the Luttinger theorem must be violated. This is the major reason why the Hubbard-I approximation has been dismissed by many authors as being unphysical.

We now wish to address the question as to what really happens if a paramagnetic (i.e. not magnetically ordered) insulator is doped away from half-filling, by QMC simulation. We therefore choose  $T = 0.33t$  and  $U = 8.0t$ . Figure 9 then shows the development of  $A(\mathbf{k}, \omega)$  with doping. It is quite obvious from this Figure that initially the 2 bands seen at half-filling in the photoemission spectrum (i.e.  $\omega < 0$ ) persist with an essentially unchanged dispersion. The chemical potential gradually cuts deeper and deeper into the topmost band, forming a hole-like Fermi surface centered on  $(\pi, \pi)$ , the top of the lower Hubbard band. The only deviation from a rather simple rigid-band behavior is an additional transfer of spectral weight: the part of the topmost band near  $(\pi, \pi)$  gains in spectral weight, whereas the band with higher binding energy loses weight. In addition, there is a transfer of weight from the upper Hubbard band to the inverse photoemission part below the Hubbard gap. This effect is actually quite well understood [20]. The band structure above the Hubbard gap becomes more diffuse upon hole doping in that the rather clear two-band structure visible near  $(\pi, \pi)$  at half-filling rapidly gives way to one broad ‘hump’ of weight. Apart from the spectral weight transfer, however, the band structure on the photoemission side is almost unaffected by the hole doping - the *dispersion* of the quasiparticle band becomes somewhat wider but does not change appreciably. In that sense we see at least qualitatively the behavior predicted by the Hubbard I approximation.

Next, we focus on the Fermi surface volume. Some care is necessary here: first, we cannot actually be sure that at the high temperature we are using there is still a well-defined Fermi surface. Second, the criterion we will be using is the crossing of the quasiparticle band through the chemical potential. It has to be kept in mind that this may be quite misleading, because band portions with tiny spectral weight are ignored in this approach (see for example Ref. [21] for a discussion). When thinking of a Fermi surface as the constant energy contour of the

chemical potential, we have to keep in mind that portions with low spectral weight may be overlooked. On the other hand the fact that a peak with appreciable weight crosses from photoemission to inverse photoemission at a certain momentum is independent of whether we call this a ‘Fermi surface’ in the usual sense, and should be reproduced by any theory which claims to describe the system. It therefore has to be kept in mind that in the following we are basically studying a ‘spectral weight Fermi surface’, i.e. the locus in  $\mathbf{k}$  space where an apparent quasiparticle band with high spectral weight crosses the chemical potential. With these *caveats* in mind, Figures 10 and 11 show the low-energy peak structure of  $A(\mathbf{k}, \omega)$  for all allowed momenta of the  $8 \times 8$  cluster in the irreducible wedge of the Brillouin zone, and for different hole concentrations. In all of these spectra there is a pronounced peak, whose position shows a smooth dispersion with momentum. Around  $(\pi, \pi)$  the peak is above  $\mu$ , whereas in the center of the Brillouin zone it is below. The locus in  $\mathbf{k}$ -space where the peak crosses  $\mu$  forms a closed curve around  $(\pi, \pi)$  and it is obvious from the Figure that the ‘hole pocket’ around  $(\pi, \pi)$  increases very rapidly with  $\delta$ . To estimate the Fermi surface volume  $V_F$  we assign a weight  $w_{\mathbf{k}}$  of 1 to momenta  $\mathbf{k}$  where the peak is below  $\mu$ , 0.5 if the peak is right at  $\mu$  and 0 if the peak is above  $\mu$ . Our assignments of these weights are given in Figures 10 and 11. The fractional Fermi surface volume then is  $V_F = \frac{1}{N} \sum_{\mathbf{k}} w_{\mathbf{k}}$ , where  $N = 64$  is the number of momenta in the  $8 \times 8$  cluster. Of course, the assignment of the  $w_{\mathbf{k}}$  involves a certain degree of arbitrariness. It can be seen from Figures 10 and 11, however, that our  $w_{\mathbf{k}}$  would in any way tend to underestimate the Fermi surface volume, so that the obtained  $V_F$  data points rather have the character of a lower bound to the true  $V_F$ . Even if we take into account some small variations of  $V_F$  due to different assignments of the weight factors, however, the resulting  $V_F$  versus  $\delta$  curve never can be made consistent with the Luttinger volume, see Figure 12. The deviation from the Luttinger volume is quite pronounced at low doping.  $V_F$  approaches the Luttinger volume for dopings  $\approx 20\%$ , but due to our somewhat crude way of determining  $V_F$  we cannot really decide when precisely the Luttinger theorem is obeyed. The Hubbard I approximation approaches the Luttinger volume for hole concentrations of  $\approx 50\%$ , i.e. the steepness of the drop of  $V_F$  is not reproduced quantitatively. The latter is somewhat improved in the so-called 2-pole approximation [13,22]. For example the Fermi surface given by Beenen and Edwards [22] for  $\langle n \rangle = 0.94$  obviously is very consistent with the spectrum in Figure 11 for  $\langle n \rangle = 0.95$ .

We return to Figure 9 and discuss the entire width of the spectra, in particular the question of the fate of the 4-band structure in the doped system. For  $\langle n \rangle = 0.95$  the different features that are seen at  $\langle n \rangle = 1.0$  are still rather clearly visible, but for  $\langle n \rangle = 0.86$  the low energy quasiparticle band at  $k = (0,0)$  starts to dis-

appear, and at  $\langle n \rangle = 0.80$  the dominant ‘band’ in the spectrum between  $\omega = -4t$  and  $\omega = 2t$  can be fitted by a slightly renormalized free-electron band. As we have seen above, the Luttinger theorem also is valid in this case. This suggests to classify the doping as ‘underdoped’ for  $0 < \langle n \rangle < 0.85$ , where the Luttinger theorem is invalid and the 4-band structure known from half-filling persists, and ‘overdoped’ where the Luttinger theorem is valid and a renormalized free-electron band can be seen in the spectral function. Following the convention for cuprate superconductors, we call the doping where the crossover between the two regimes occurs the ‘optimal’ doping.

Next, the four plots of figure 13 show the spectra at selected  $\mathbf{k}$ -points. The system size is only  $6 \times 6$  in this case because this allows for smaller error bars. Closer inspection, especially, of the peaks at momentum  $\mathbf{k} = (0, 0)$  on the photoemission side (plot (a)) and at momentum  $\mathbf{k} = (\pi, \pi)$  on the inverse photoemission side (plot (d)) confirms, that with increasing hole concentration we are losing parts of the 4-band structure seen at half-filling.

To check the physics of the band structure in more detail, we again employ our diagnostic operators. Figure 14 shows the angle-resolved spectral functions  $\tilde{A}(\mathbf{k}, \omega)$  of the spin-1/2 and spin-3/2 string operators,  $b_{i,\uparrow}$  and  $\tilde{b}_{i,\uparrow}$ . As was the case at half-filling, the spectrum of the spin-1/2 string operator highlights exactly those peaks that we associate with the dispersionless ‘dressed hole’ bands in Figure 5. The spectrum of the spin-3/2 string operator on the other hand has its peaks with maximal spectral weight around momentum  $\mathbf{k} = (\pi, \pi)$ , indicating that also in the doped case there is an ‘antiferromagnetic mirror image’ of the quasiparticle band (which, however, consists of spin-3/2 states). Again, coupling of photoholes to thermally excited spin excitations may make these states visible in ARPES spectra, thus explaining the ‘shadow bands’ seen in photoemission experiments by Aebi *et al.* [23]. Similarly as for half-filling one might speculate that a magnetic field, which would break spin symmetry and thus allow for a coupling of ‘bands’ with different total spin, would enhance the spectral weight of these shadow bands.

All in all we have seen that the ‘band structure’ (4-band structure, dispersion of regions of large spectral weight, ‘character’ of the bands as measured by the diagnostic operators) stays pretty much unchanged as long as we are in the underdoped regime. At half-filling the 4-band structure is closely related to the sharp low-energy mode in the dynamical spin correlation function, which naturally suggests to study the spin response also as a function of doping. Figure 15 shows the spin-correlation function,  $\chi_{sz}(\mathbf{k}, \omega)$  (left column), and the charge-correlation function,  $\chi_{cc}(\mathbf{k}, \omega)$  (right column), for  $T = 0.33t$  and densities  $\langle n \rangle = 0.95$  (underdoped),  $\langle n \rangle = 0.90$  (nearly optimally doped) and  $\langle n \rangle = 0.80$  (overdoped). The

spin-response is sharply confined in both momentum  $\mathbf{k} = (\pi, \pi)$  and energy  $\omega = \omega^*$  only in the underdoped region i.e. the regime where we also observe the features associated with spin excitations in the single-particle spectra. As was the case at half-filling for temperatures below  $T \approx 0.33t$ , the spin-response can be fitted by the AF spin-wave dispersion (19) in the underdoped regime. On the other hand, as soon as the system enters the overdoped regime the spin-response is no longer sharply peaked at momentum  $\mathbf{k} = (\pi, \pi)$  and energy  $\omega = \omega^*$ : it broadens in momentum and spreads in energy by an order of magnitude with the scale changing from  $J = 4t^2/U$  to  $E_{kin} \sim 8.0t$  accompanied by a similar change in the bandwidth of the single particle excitations. This result is already well known from previous QMC calculations [26] and consistent with similar behaviour in the t-J model [28]. The charge-response,  $\chi_{cc}(\mathbf{k}, \omega)$ , is always broad in both momentum  $\mathbf{k}$  and energy  $\omega$  for all densities studied. It merely decreases its width from  $\approx 12.0t$  at  $\langle n \rangle = 0.95$  to  $\approx 8.0t$  at  $\langle n \rangle = 0.80$ .

Although the minus-sign problem of the QMC algorithm prevents reliable simulations of large systems at low temperatures in the doped regime, we nevertheless studied the temperature evolution of the angle-resolved spectral function  $A(\mathbf{k}, \omega)$  at density  $\langle n \rangle = 0.93$ . This was possible due to the relative small system size of  $6 \times 6$ , which alleviates the minus-sign problem as compared to  $8 \times 8$  at the  $T = 0.25t$ . Figure 16 shows the results from this analysis: the uppermost plot (a) compares the angle-resolved spectral functions  $A(\mathbf{k}, \omega)$  at density  $\langle n \rangle = 0.93$  for  $T = 0.50t$ ,  $T = 0.33t$  and  $T = 0.25t$ . We stress that the simulation at  $T = 0.25t$  suffers from minus-sign problems with a drastically reduced resolution. In the center plot (b), the quasiparticle peak weights around momentum  $\mathbf{k} = (\pi, \pi)$  of the  $\langle n \rangle = 0.93$  simulation are compared with the quasiparticle peak weight at momentum  $\mathbf{k} = (\pi, \pi)$  of a half-filled,  $\langle n \rangle = 1.0$ , simulation for different temperatures. At half-filling, the Hubbard-I-like quasiparticle peak  $\mathbf{k} = (\pi, \pi)$  and  $\omega \approx -1.5t$  decreases in spectral weight with decreasing  $T$  and disappears as the spin-correlation length (which increases with decreasing temperature) reaches the lattice size (at  $T \approx 0.20t$ ). In the underdoped case for density  $\langle n \rangle = 0.93$  the weights of the corresponding peaks around momentum  $\mathbf{k} = (\pi, \pi)$  located also decrease with decreasing  $T$ . Closer inspection of this peak (see the inset of the center plot (b)) reveals, that this peak even raises slightly in binding energy with decreasing temperature, very similar to the peak in the half-filled case. In a real photoemission experiment this peak would have dropped below the typical resolution of roughly 10% spectral weight [27] at a temperature of  $T \approx 0.25t$ . The spin-correlation length (again derived by a fit of the equal-imaginary-times spin-correlation function to a form  $a \cdot |\mathbf{r}|^b \cdot e^{-|\mathbf{r}|/\zeta_{sz}(T)}$ ) also shows similar behavior in the underdoped and half-filled cases: the values for the spin-correlation length are  $\zeta_{sz} = 0.5 - 0.8$ ,

$\zeta_{sz} = 0.8 - 1.0$  and  $\zeta_{sz} = 1.0 - 1.3$  in the underdoped case and  $\zeta_{sz} = 0.6 - 0.9$ ,  $\zeta_{sz} = 1.0 - 1.3$  and  $\zeta_{sz} = 1.6 - 1.9$  at half-filling for  $T = 0.50t$ ,  $T = 0.33t$  and  $T = 0.25t$ , respectively. The spin-susceptibility (shown in plot (c) of figure 16) also behaves very similar, but with changed magnitudes in the underdoped and in the half-filled cases. These data suggest a similar temperature evolution of the band-structure of the Hubbard model in the underdoped and half-filled cases driven by the temperature dependent spin-correlation length  $\zeta_{sz}(T)$ . Especially, we expect the Hubbard-I-like quasiparticle peaks at energies of  $\omega \approx 1.0t$  around momentum  $\mathbf{k} = (\pi, \pi)$  to vanish with decreasing  $T$  in the underdoped case as the peaks at energies of  $\omega \approx -1.5t$  around momentum  $\mathbf{k} = (\pi, \pi)$  do in the case of half-filling.

The latter observation suggests a profound change of the Fermi surface with temperature: as seen above, it is precisely the Hubbard-I-like band near  $(\pi, \pi)$  which crosses the chemical potential and thus forms the Fermi surface in the doped case. It is then quite clear that the ‘disappearance’ of this band with decreasing temperature must affect the Fermi surface in some dramatic way. Studies at zero temperature are possible only by means of exact diagonalization. Analysis of the single particle spectrum shows the same ‘rigid-band’ behaviour as at high temperatures [29] and analysis of the momentum distribution  $n(\mathbf{k})$  suggest [30] that the doped holes accumulate at the surface of the magnetic zone (i.e. the line  $(\frac{\pi}{2}, \frac{\pi}{2}) \rightarrow (\pi, 0)$ ) rather than around  $(\pi, \pi)$ .

## V. SUMMARY

In the present work we have systematically studied the temperature- and doping-dependent dynamics of the two-dimensional Hubbard model by finite-temperature QMC simulations. Comparing the QMC single particle spectral function, the dynamical spin response and the spectral functions of suitably chosen diagnostic operators, different physical regimes could be identified. In simplest terms there are two quantities, which basically determine the single particle spectrum: the hole concentration and the spin-response function, whereby there is a certain relationship between the two.

At half-filling and high temperatures ( $T \geq t$ ), the combined photoemission and inverse photoemission spectrum  $A(\mathbf{k}, \omega)$  displays two dispersive features, the upper and lower Hubbard band, roughly separated by  $U$  ( $= 8t$ , in our work). At these very high temperatures the system is in a spin disordered state. We have demonstrated here that the well-known Hubbard-I approximation gives an excellent description of the single particle spectrum in this state, reproducing quantitatively both the single-particle dispersion and the distribution of spectral weight. This is by no means trivial, since the Hubbard-I approximation is dynamically equivalent

to a simplified effective Hamiltonian, which just contains hole-like ( $h_{i,\sigma}^\dagger$ ) and double occupancy-like particles in a simple bi-quadratic form.

At lower temperatures ( $T \leq 0.33t$ ), the Hubbard-I approximation needs to be improved; this is to be expected, because it neglects all effects of spin-correlations. In fact, the temperature where deviations from Hubbard-I become strong, coincides fairly well with the transition from a spin response  $\chi_{sz}(\mathbf{k}, \omega)$  which is diffuse both in momentum and energy (with a spread of order  $t$ ), to a more ‘spin-wave-like’ response. In this regime  $\chi_{sz}(\mathbf{k}, \omega)$  displays the characteristic energy scale  $J = 4t^2/U$ , with its spectral weight being concentrated at the AF wave vector  $\mathbf{Q} = (\pi, \pi)$ . It should be noted that this ‘spin-wave-like’ regime develops despite the fact that at  $T = 0.33t$  the spin-correlations length  $\zeta_{sz}(T)$  is still short-ranged ( $\leq 2$  lattice spacings). Only at the lower temperature  $T = 0.10t$  Néel order spreads over the entire QMC block, creating an effective (finite-size) Néel state.

It is well established by previous, in particular also QMC work, that in this temperature-regime ( $T \leq 0.33t$ ) new spectral features appear. They have often been interpreted as four ‘bands’, two ‘coherent’ bands forming the topmost valence and the lowest conduction band in the insulator plus two ‘incoherent’ bands, i.e. the remaining upper and lower Hubbard band features (see for example [12]). Our present work not only definitively identifies these four bands but also clarifies their physical origin and their connection to the spin-excitations. In simplest terms the emerging spin waves at lower temperatures provide the excitations that can ‘dress’ the Hubbard quasiparticles, whence new bands corresponding to dressed holes/double occupancies appear in the single particle spectrum  $A(\mathbf{k}, \omega)$ . It has been shown in Ref. [11] that the 4-band structure which appears in  $A(\mathbf{k}, \omega)$  at lower temperatures can be explained in this way, and our present numerical check by directly calculating the spectra of ‘dressed electrons’ supports this interpretation. This physical picture at half-filling can be extended into the underdoped regime. This is most obvious in the single particle spectral function, which stays almost unchanged in the doped case (i.e. the 4-band structure and the ‘character’ of the bands as measured by the diagnostic operators). The main change in fact consists in the chemical potential cutting gradually into the (top of the) lower Hubbard band, precisely as predicted by the Hubbard-I approximation. Contrary to widespread belief the ‘Fermi surface’, if determined by the Fermi surface crossings of the dominant band through the chemical potential, does not satisfy the Luttinger theorem. Rather, for small hole concentrations the Fermi surface volume is considerable larger than that for a slightly less than half-filled free-electron band. Very similar conclusions have in fact been reached by a calculation of the electron momentum distribution in the 2D t-J model by Puttিকা *et al.* [31]. Their calculation actually was a high temperature series expansion

sion plus a Padé extrapolation to lower temperature, and it is encouraging that this method gives similar results as our QMC results which are performed at relatively high temperatures. In its range of applicability, i.e. in the absence of strong magnetic correlations and close to half-filling, the Hubbard-I approximation thus works remarkably well, both at half-filling and in the doped case. We stress that this has profound implications for the theoretical treatment of the model: perturbation expansions in  $U$  or partial and self-consistent resummations thereof, may not be expected to give any meaningful results in this strong-coupling/low doping regime.

An interesting question is the possibility to verify our results experimentally. As already mentioned above, a scan of the temperature development of  $A(\mathbf{k}, \omega)$  shows that the part of the quasiparticle band near  $(\pi, \pi)$  (where the Fermi surface is located) is loosing weight with decreasing temperature. In fact in ARPES experiments on underdoped cuprate superconductors the ‘hole-pocket’ around  $(\pi, \pi)$  seen in our simulations (and the expansion of Puttিকা *et al.*) is not observed, but rather a small ‘Fermi arc’ near  $(\pi/2, \pi/2)$ , terminated by the ‘pseudo gap’ around  $(\pi, 0)$  Although our simulations do not allow to make statements about the truly low temperatures in the experiments, we believe that this suggests a strong temperature dependence of the single particle spectrum, with the temperature scale being set by the exchange constant  $J$  (which controls the degree of spin disorder). The latter is rather large in copper oxides, so that the temperature regime studied in our simulations probably cannot be accessed experimentally in these materials. We note, however, that an ARPES study for the 1D material  $Na_{0.96}V_2O_5$  which has a smaller exchange constant, has indeed provided evidence for a strong  $T$ -dependence of  $A(\mathbf{k}, \omega)$  [32]. Clearly, it would be interesting to study the Fermi surface evolution in a 2D material with lower exchange constant.

As was the case at half-filling, the dynamical spin-response plays an important role: throughout the Hubbard-I phase at low doping, the spin response shows the sharp low-energy mode at  $(\pi, \pi)$ . The simultaneous disappearance of the 4-band structure in  $A(\mathbf{k}, \omega)$  and the low energy spin response with scale  $J$  in the overdoped regime then show again the close relationship between the two. The dressing of holes by spin excitations apparently remains the most important correction over Hubbard-I. In the overdoped regime the spin response is spread out over an energy range of  $\approx 8t$  and thus becomes more similar to the charge response. The single-particle spectral function is most consistent with a slightly renormalized free electron dispersion, and the Luttinger theorem appears to be satisfied even at the relatively high temperature  $T = 0.33t$ . This is quite consistent with earlier results on the t-J model, which show that for hole concentrations  $\geq 25\%$  the spin and charge response can be approximated well by the self-convolution of the single par-

ticle spectral function [33]. This is essentially what is to be expected for a system of weakly interacting Fermions, so that we conclude that in the overdoped regime we enter a new phase which most probably extends to the low-concentration limit where the Nagaoka  $T$ -matrix approximation becomes exact. Finally we note that exact diagonalization studies at finite temperatures [34] also show some evidence for a ‘crossover’ between different physical regimes at a hole concentration of 15%.

This work was supported by DFN Contract No. TK 598-VA/D03 and by BMBF (05SB8WWA1). Computations were performed at HLRS Stuttgart and HLRZ Jülich. One of us (W.H.) acknowledges hospitality of the Physics Department in Santa Barbara and many useful discussions with D. J. Scalapino.

- 
- [1] E. Loh and J. Gubernatis, *Electronic Phase Transitions*, W. Hanke and Y. V. Kopaev, North Holland, Amsterdam (1992).
  - [2] J. E. Hirsch, Phys. Rev. B **31**, 4403 (1985).
  - [3] M. Jarrel, J. E. Gubernatis, Phys. Rep. **269**, 133 (1996).
  - [4] E. Fradkin, *Field Theories of Condensed Matter Systems*, Frontiers in Physics, Addison-Wesley Publishing Company (1991).
  - [5] N. D. Mermin and H. Wagner, Phys. Rev. Lett. **17**, 1133 (1966).
  - [6] A. B. Harris and R. V. Lang, Phys. Rev. **157**, 295 (1967).
  - [7] J. R. Schrieffer, X.-G. Wen, and S.-C. Zhang, Phys. Rev. Lett. **60**, 944 (1988).
  - [8] J. R. Schrieffer, X.-G. Wen, and S.-C. Zhang, Phys. Rev. B **39**, 11663 (1989).
  - [9] L. N. Bulaevskii, E. L. Nagaev, and D. I. Khomskii, Sov. Phys. JETP **27**, 638 (1967); S. A. Trugman, Phys. Rev. B **37**, 1597 (1988); *ibid.* **41**, 892 (1990); R. Eder and K. W. Becker, Z. Phys. B **78**, 219 (1990); O. P. Sushkov, Solid State Commun. **83**, 303 (1992); A. Ramsak and P. Horsch, Phys. Rev. B **48**, 10559 (1993); G. Reiter, Phys. Rev. B **49**, 1536 (1994); R. Hayn, A. F. Barabanov, J. Schulenburg, and J. Richter, Phys. Rev. B **53**, 11714 (1996).
  - [10] J. Hubbard, Proc. Roy. Soc. A **276**, 238 (1963).
  - [11] A. Dorneich, M. G. Zacher, C. Gröber and R. Eder, e-print cond-mat/
  - [12] R. Preuss, W. Hanke, and W. v. d. Linden, Phys. Rev. Lett. **75**, 1344 (1995).
  - [13] B. Mehlig, H. Eskes, R. Hayn, and M. B. J. Meinders, Phys. Rev. B **52**, 2463 (1995).
  - [14] E. Dagotto, F. Ortolani, and D. Scalapino, Phys. Rev. B **46**, 3183 (1992).
  - [15] C. N. Yang, Phys. Rev. Lett. **63**, 2144 (1989); S. C. Zhang, Phys. Rev. Lett. **65**, 120 (1990).
  - [16] E. Dagotto and J. R. Schrieffer, Phys. Rev. B **43**, 8705 (1991).
  - [17] R. Eder and Y. Ohta, Phys. Rev. B **50**, 10043 (1994).

- [18] A. L. Fetter and J. D. Walecka, *Quantum Theory of Many-Particle Systems*, McGraw-Hill, New York (1971).
- [19] F. Ronning, C. Kim, D. L. Feng, D. S. Marshall, A. G. Loeser, L. L. Miller, J. N. Eckstein, I. Bozovic, Z.-X. Shen, *Science* **282**, 2067 (1998).
- [20] H. Eskes and A. M. Oles, *Phys. Rev. Lett.* **73** 1279 (1994).
- [21] R. Eder and Y. Ohta, *Phys. Rev. Lett.* **72**, 2816 (1994).
- [22] J. Beenen and D. M. Edwards, *Phys. Rev. B* **52**, 13636 (1995).
- [23] P. Aebi, J. Osterwalder, P. Schwaller, L. Schlapbach, M. Shimoda, T. Mochiku, and K. Kadowaki, *Phys. Rev. Lett.* **72**, 2757 (1994).
- [24] L. M. Roth, *Phys. Rev.* **184**, 451 (1969).
- [25] G. Geipel and W. Nolting, *Phys. Rev. B* **38**, 2608 (1988); W. Nolting and W. Borgiel, *Phys. Rev. B* **39**, 6962 (1989).
- [26] R. Preuss, W. Hanke, C. Gröber, and H. G. Evertz, *Phys. Rev. Lett.* **79**, 1122 (1997).
- [27] S. Haas, A. Moreo, and D. Dagotto, *Phys. Rev. Lett.* **74**, 4281 (1995).
- [28] J. Jaklic and P. Prelovsek, *Phys. Rev. Lett.* **74**, 3411 (1995).
- [29] R. Eder, Y. Ohta, and T. Shimozato, *Phys. Rev. B* **50**, 3350 (1994).
- [30] S. Nishimoto, Y. Ohta, and R. Eder, *Phys. Rev. B* **57**, 5590 (1998).
- [31] W. O. Putikka, M. U. Luchini, and R. R. P. Singh, *Phys. Rev. Lett.* **81**, 2966 (1998).
- [32] K. Kobayashi, T. Mizokawa, A. Fujimori, M. Isobe, Y. Ueda, T. Tohyama, S. Maekawa, *Phys. Rev. Lett.* **82**, 803 (1999).
- [33] R. Eder and Y. Ohta, *Phys. Rev. B* **51**, 11683 (1994).
- [34] J. Jaklic and P. Prelovsek, *Phys. Rev. Lett.* **77**, 892 (1996).

FIG. 1. Angle-resolved spectral function  $A(\mathbf{k}, \omega)$  of a  $8 \times 8$  Hubbard lattice at  $\langle n \rangle = 1.0$  and  $U = 8.0t$  for various temperatures. The solid lines in the left column represent the (renormalized) Hubbard-I and SDW dispersions. In the right column the spectral functions from QMC (solid lines) are compared to the Hubbard-I and SDW-approximations with a Lorentzian lineshape (dashed lines).

FIG. 2. Dynamical spin-correlation function,  $\chi_{sz}(\mathbf{k}, \omega)$  (left column), and charge-correlation functions  $\chi_{cc}(\mathbf{k}, \omega)$  (right column), of a  $8 \times 8$  Hubbard lattice at  $\langle n \rangle = 1.0$  and  $U = 8.0t$  for  $T = 1.00t$ ,  $T = 0.33t$  and  $T = 0.10t$ . The solid lines in the lower left column give a spin-wave fit.

FIG. 3. Angle-resolved spectral function  $\tilde{A}(\mathbf{k}, \omega)$  of the shadow-operator  $\tilde{c}_{i,\sigma}$  with  $8 \times 8$  lattice size at  $\langle n \rangle = 1.0$  and  $U = 8.0t$  for  $s T = 0.33t$  and  $T = 0.10t$ .

FIG. 4. Single-particle spectral function of the normal photoemission (top) and the shadow-operator (bottom) at momentum  $\mathbf{k} = (\pi, \pi)$  with  $8 \times 8$  lattice size at  $\langle n \rangle = 1.0$  and  $U = 8.0t$  for temperatures in between  $T = 1.00t$  and  $T = 0.10t$ .

FIG. 5. Angle-resolved spectral function  $A(\mathbf{k}, \omega)$  of the  $8 \times 8$  Hubbard lattice with  $U = 8.0t$  for  $T = 0.33t$  (top) and  $T = 0.10t$  (bottom) compared to analytic dispersions: mixing the Hubbard-I (top, dashed) or SDW (bottom, dashed) bands with two dispersionless bands at  $\omega = \pm 3t$  (dashed) results in a 4-band structure (solid) in good agreement with the QMC peaks.

FIG. 6. Motion of an added hole in an Néel state (left) and an RVB state (right) produces spin defects of different kind. These are described by the spin-1/2 string operator.

FIG. 7. Angle-resolved spectral function  $\tilde{A}(\mathbf{k}, \omega)$  of the spin-1/2 string operator  $b_{i,\uparrow}$  in the Hubbard model with  $U = 8.0t$  for  $T = 0.33t$  (top) and  $T = 0.10t$  (bottom). The lattice size was reduced to  $6 \times 6$  in this case due to the larger error bars of the string operator as compared to the normal photoemission spectrum.

FIG. 8. Angle-resolved spectral function  $\tilde{A}(\mathbf{k}, \omega)$  of the spin-3/2 string operator  $\tilde{b}_{i,\uparrow}$  in the Hubbard model with  $U = 8.0t$  for  $T = 0.33t$  (top) and  $T = 0.10t$  (bottom). The lattice size was reduced to  $6 \times 6$  in this case due to the larger error bars of the quartet operator as compared to the normal photoemission spectrum.

FIG. 9. Overview on the doping dependence of the angle-resolved spectral function  $A(\mathbf{k}, \omega)$  of the  $8 \times 8$  Hubbard lattice at  $T = 0.33t$  and  $U = 8.0t$  for densities  $\langle n \rangle = 1.00$  (half-filled),  $\langle n \rangle = 0.95$  (underdoped),  $\langle n \rangle = 0.86$  (roughly optimal doped) and  $\langle n \rangle = 0.80$  (overdoped).

FIG. 10. Single particle spectral function for all  $\mathbf{k}$ -points of the  $8 \times 8$  cluster in the irreducible wedge of the Brillouin zone. For each  $\mathbf{k}$  the weight  $w_{\mathbf{k}}$  is given.

FIG. 11. Same as Figure 10 for lower electron densities.

FIG. 12. Fermi surface volume as estimated from the single particle spectral function, plotted versus the concentration of holes in the half-filled band. The dashed line gives the value predicted by the Luttinger theorem,  $V_F = \frac{\pi}{2}$ .

FIG. 13. Angle-resolved spectral function  $A(\mathbf{k}, \omega)$  of a  $6 \times 6$  Hubbard lattice at  $T = 0.33t$  and  $U = 8.0t$  for momenta  $\mathbf{k} = (0, 0)$  (plot (a)) and  $\mathbf{k} = (\pi, 0)$  (plot (b)) and  $\mathbf{k} = (\pi, \pi)$  (plot (c) and (d)). The spectra for the various densities  $\langle n \rangle = 1.00$ ,  $\langle n \rangle = 0.96$ ,  $\langle n \rangle = 0.90$ ,  $\langle n \rangle = 0.83$  and  $\langle n \rangle = 0.66$  are shifted by their individual chemical potentials  $\mu$  resulting in overlapping peaks in the underdoped regime. The labels at the  $\omega$ -axis refer to the half-filled simulation (solid line). The system size is  $6 \times 6$ , because the smaller errors in this case lead to more reliable spectra.

FIG. 14. Angle-resolved spectral function  $\tilde{A}(\mathbf{k}, \omega)$  of the spin-1/2 string operator  $b_{i,\uparrow}$  (top) and the spin-3/2 string operator  $\tilde{b}_{i,\uparrow}$  (bottom) in the Hubbard model with  $U = 8.0t$  for  $T = 0.33t$  and densities  $\langle n \rangle = 0.95$  (left) and  $\langle n \rangle = 0.90$  (right). The lattice size was  $6 \times 6$  in this case due to the larger error bars of the string operators as compared to the normal photoemission spectrum.

FIG. 15. Dynamical spin-,  $\chi_{sz}(\mathbf{k}, \omega)$  (left column), and charge-correlation functions,  $\chi_{cc}(\mathbf{k}, \omega)$  (right column), of a  $8 \times 8$  Hubbard lattice at  $U = 8.0t$  and  $T = 0.33t$  for densities  $\langle n \rangle = 0.95$ ,  $\langle n \rangle = 0.90$  and  $\langle n \rangle = 0.80$ . The solid lines in the upper plots of the left column give a spin-wave fit.

FIG. 16. (a) Angle-resolved spectral function  $A(\mathbf{k}, \omega)$  of the  $6 \times 6$  Hubbard lattice with  $U = 8.0t$  and density  $\langle n \rangle = 0.93$  versus  $T$ , (b) quasiparticle peak weight around momentum  $\mathbf{k} = (\pi, \pi)$  for  $\langle n \rangle = 1.0$  ( $8 \times 8$ ) and  $\langle n \rangle = 0.93$  ( $6 \times 6$ ) versus  $T$  and (c) magnetic susceptibility  $\chi_{sz}(\mathbf{k} = (\pi, \pi), \omega = 0)$  for densities  $\langle n \rangle = 1.0$  ( $8 \times 8$ ) and  $\langle n \rangle = 0.93$  ( $6 \times 6$ ) versus  $T$ . Please note the slightly raising (in binding energy) and vanishing (in spectral weight) with decreasing temperature of the peak located at  $\mathbf{k} = (\pi, \pi)$  magnified in the inset of plot (b). The system size is only  $6 \times 6$  in the doped case to avoid the serious sign problems of the  $8 \times 8$  system at  $T = 0.25t$ . But also the  $6 \times 6$  data at  $T = 0.25t$  suffer from sign problems at some momenta,  $\mathbf{k} = (0, 0)$  and  $\mathbf{k} = (\pi/3, 0)$ .

This figure "fig1.gif" is available in "gif" format from:

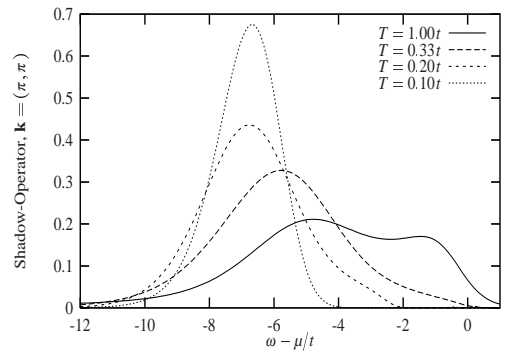
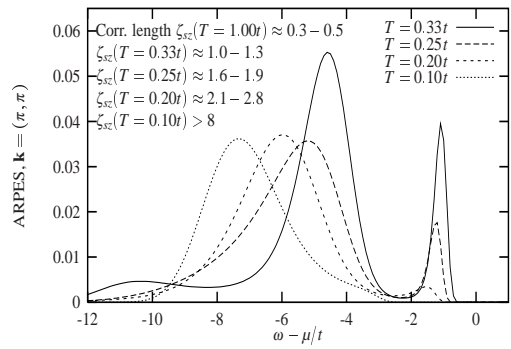
<http://arxiv.org/ps/cond-mat/0001366v1>

This figure "fig2.gif" is available in "gif" format from:

<http://arxiv.org/ps/cond-mat/0001366v1>

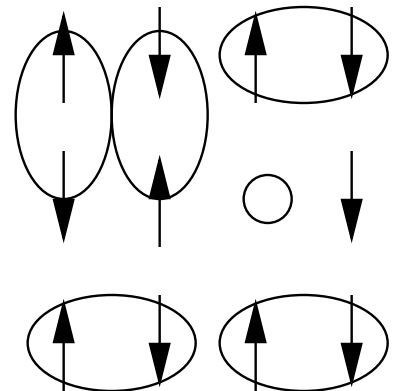
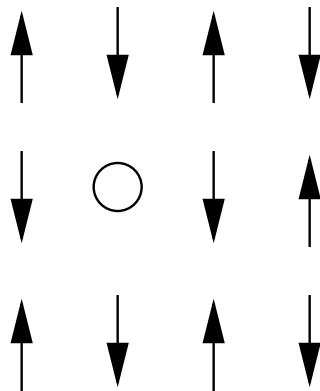
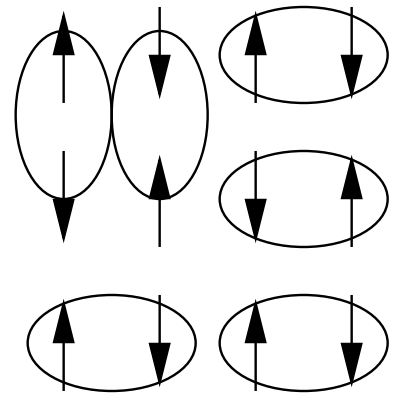
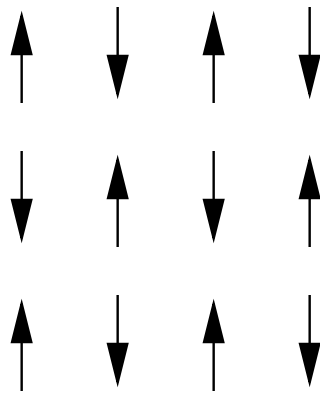
This figure "fig3.gif" is available in "gif" format from:

<http://arxiv.org/ps/cond-mat/0001366v1>



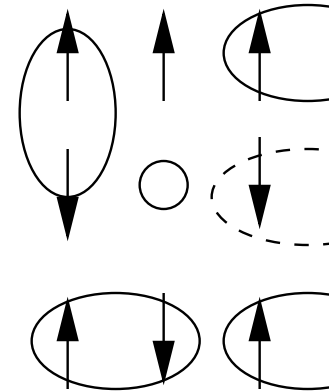
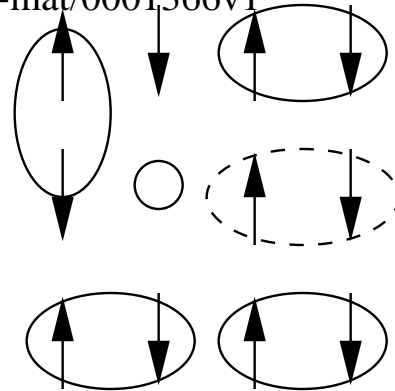
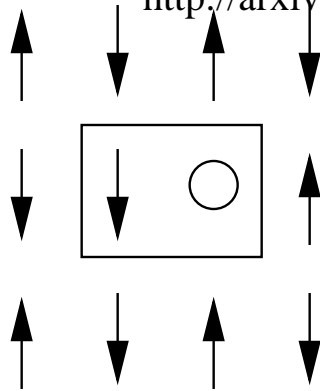
This figure "fig5.gif" is available in "gif" format from:

<http://arxiv.org/ps/cond-mat/0001366v1>



This figure "fig7.gif" is available in "gif" format from:

<http://arxiv.org/ps/cond-mat/0001366v1>



Néel

RVB

This figure "fig8.gif" is available in "gif" format from:

<http://arxiv.org/ps/cond-mat/0001366v1>

This figure "fig9.gif" is available in "gif" format from:

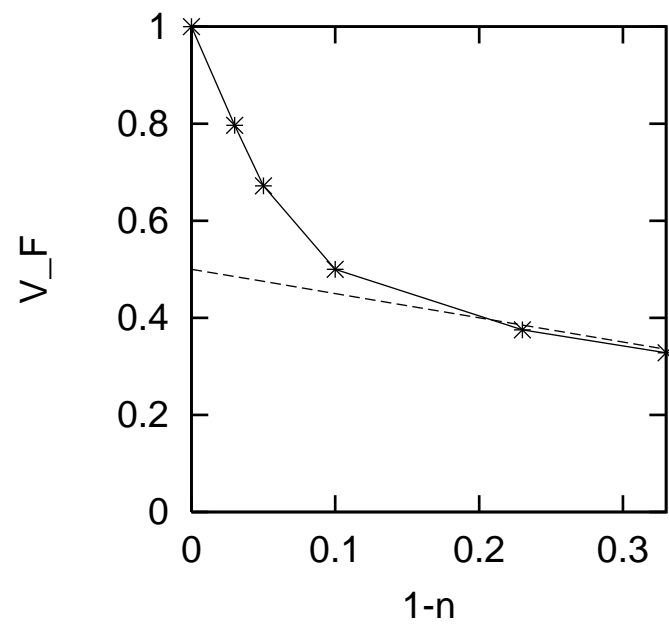
<http://arxiv.org/ps/cond-mat/0001366v1>

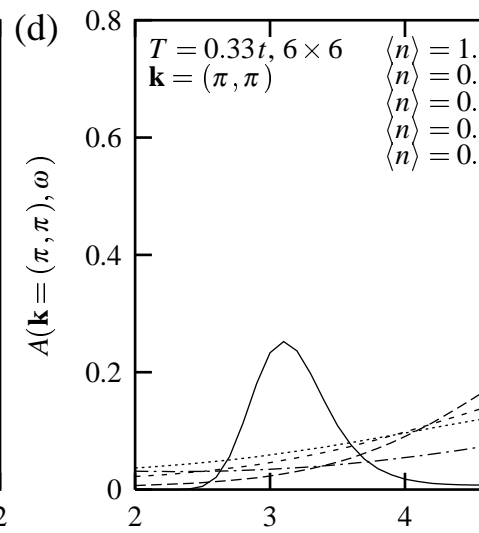
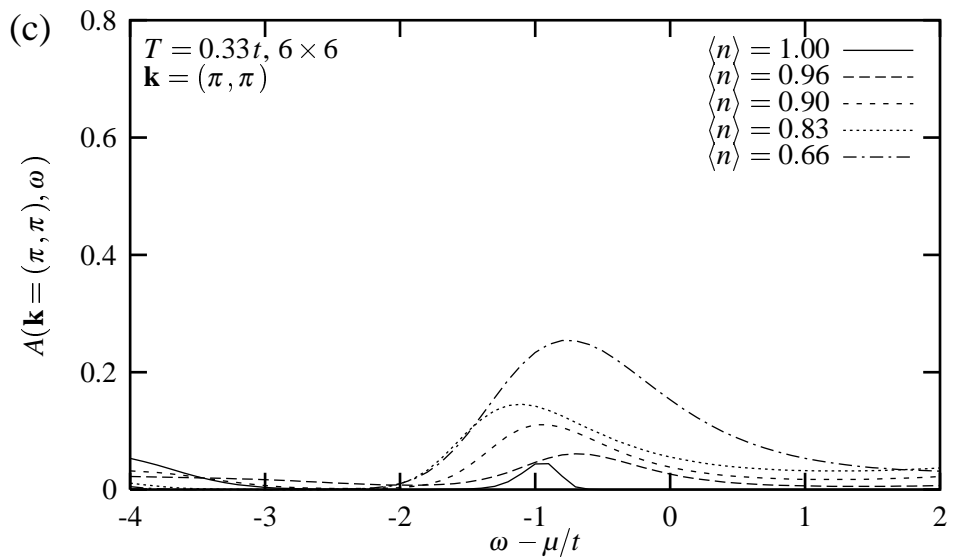
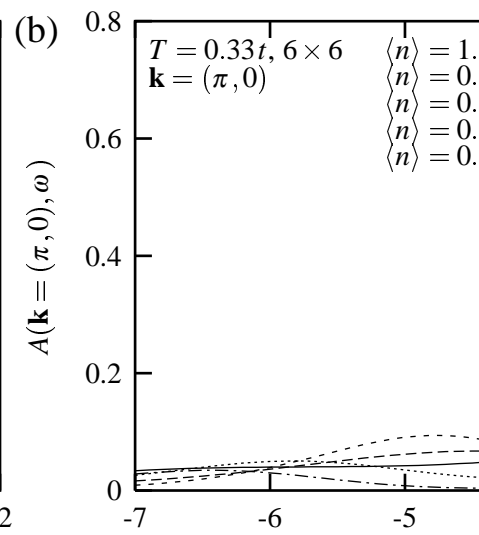
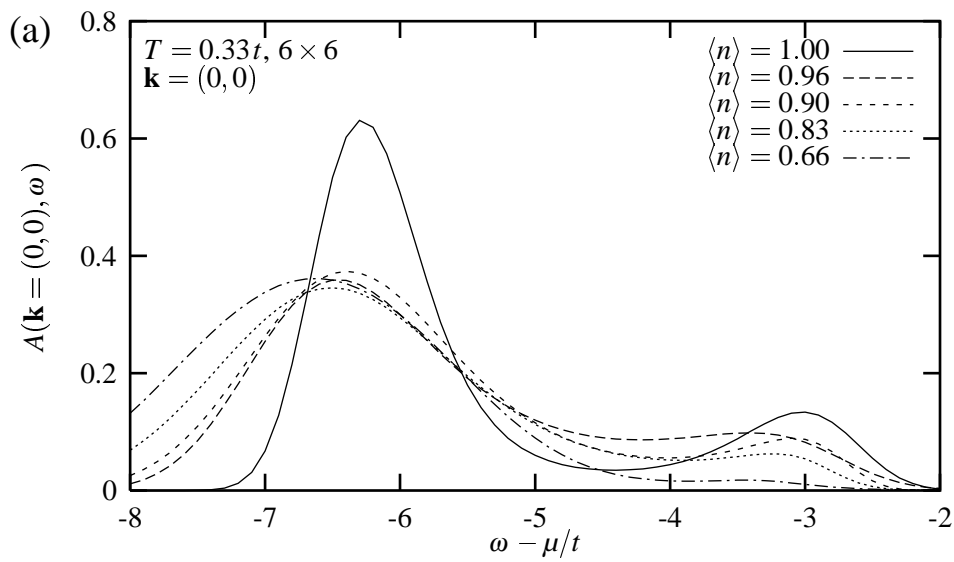
This figure "fig10.gif" is available in "gif" format from:

<http://arxiv.org/ps/cond-mat/0001366v1>

This figure "fig11.gif" is available in "gif" format from:

<http://arxiv.org/ps/cond-mat/0001366v1>





This figure "fig14.gif" is available in "gif" format from:

<http://arxiv.org/ps/cond-mat/0001366v1>

This figure "fig15.gif" is available in "gif" format from:

<http://arxiv.org/ps/cond-mat/0001366v1>

